Materials **2012**, *5*, 1275-1284; doi:10.3390/ma5071275

OPEN ACCESS

materials

ISSN 1996-1944

www.mdpi.com/journal/materials

Article

Self-Assembly of Bi_2Te_3-Nanoplate/Graphene-Nanosheet Hybrid by One-Pot Route and Its Improved Li-Storage Properties

Fangfang Tu, Jian Xie *, Gaoshao Cao and Xinbing Zhao

State Key Laboratory of Silicon Materials, Department of Materials Science and Engineering, Zhejiang University, Hangzhou 310027, China; E-Mails: fangfangtu1990@126.com (F.T.); gscao@zju.edu.cn (G.C.); zhaoxb@zju.edu.cn (X.Z.)

* Author to whom correspondence should be addressed; E-Mail: xiejian1977@zju.edu.cn; Tel.: +86-571-8795-2181; Fax: +86-571-8795-1451.

Received: 12 June 2012; in revised form: 5 July 2012 / Accepted: 10 July 2012 / Published: 23 July 2012

Abstract: A sandwich structured Bi_2Te_3-nanoplates/graphene-nanosheet (Bi_2Te_3/G) hybrid has been synthesized by a facile in situ solvothermal route and has been investigated as a potential anode material for Li-ion batteries. Bi_2Te_3 grows during the solvothermal process with the simultaneous reduction of graphite oxide into graphene. The in situ formation process of the hybrid has been investigated by X-ray diffraction and X-ray photoelectron spectra. The Li-storage mechanism and performance of Bi_2Te_3/G and bare Bi_2Te_3 have been studied by galvanostatic cycling and cyclic voltammetry. The Bi_2Te_3/G sandwich exhibits an obviously improved cycling stability compared to bare Bi_2Te_3. The enhancement in electrochemical performance can be attributed to the combined conducting, confining and dispersing effects of graphene for Bi_2Te_3 nanoplates and to the self-assembled sandwich structure.

Keywords: bismuth telluride; graphene; Li-ion batteries; sandwich

1. Introduction

Although carbon based materials are presently the dominant anodes in commercial Li-ion batteries, there is still a great challenge to develop alternative anode materials in order to meet the requirement of high-performance Li-ion batteries [1,2]. Alloy materials have been regarded as one of the most promising anodes for the next-generation Li-ion batteries because of their safe operating voltage and

the large energy density, especially the large volumetric energy density due to the high density [3,4]. Among various elements that can form Li-alloys, Sb has received a special interest because of its appropriate alloying/de-alloying voltage (around 0.8 V *vs.* Li/Li^+) and relatively large Li-storage capacity (660 mAh g^{-1}) with the formation of Li_3Sb composition [5]. However, the volume change is over 200% during the conversion from Sb to Li_3Sb [6]. The volume change causes the cracking and crumbling of the particles, resulting in the loss of physical contact between the active particles and the current collector and the consequent capacity loss upon cycling.

Many measures have been taken to alleviate the volume changes for Sb during alloying/de-alloying processes. Previous work [7–10] showed that the cycling stability of metallic Sb can be improved by using Sb-based intermetallic compound MSb_x, where M is an electrochemically inert element and acts as the buffering matrix. The improvement in electrochemical performance could also be realized by using nanostructured materials [11–14] due the large surface area, short Li-ion diffusion path and increased mechanical strength. However, the nanoparticles tend to aggregate, also leading to the disconnection of active material with the current collector. An effective approach to overcome this problem is to immobilize the nanoparticles on a matrix. Carbon-based materials [15–18] are considered as the ideal matrices since they are electrically conductive and electrochemically active in addition to the buffering effect for the volume change.

Graphene, a flat monolayer of sp^2-bonded carbon atoms [19], was also the ideal matrix because of its appealing properties such as high electronic conductivity [20], high specific surface area [21] and high mechanical strength [22]. Our previous work showed that the cycling stability of some Sb-based intermetallic compounds could be improved by forming nanocomposites with graphene [23,24]. Similar to Sb, Bi in the same group can also electrochemically store Li by forming a Li_3Bi composition [5,25–27]. So far, the effect of graphene on the electrochemical performance of Bi-based anodes has not been reported yet. Herein, an in situ solvothermal route was used to prepare the Bi_2Te_3-nanoplate/graphene-nanosheet (Bi_2Te_3/G), where Te can also reversibly store Li by forming Li_2Te [27]. The results showed that an obvious improvement in cycling stability of Bi_2Te_3 could be realized by constructing a Bi_2Te_3/G hybrid with a sandwich structure.

2. Results and Discussion

Figure 1a shows the XRD patterns of Bi_2Te_3/G and bare Bi_2Te_3. For comparison, the standard diffraction peaks of Bi_2Te_3 are also given. All the diffraction peaks can be indexed to hexagonal Bi_2Te_3 (JCPDS No. 89-2009) for both Bi_2Te_3/G and bare Bi_2Te_3. The diffraction peaks of graphene that should appear at around 2θ = 25 °C cannot be detected, suggesting that the restacking of graphene sheets after reduction was inhibited by uniformly loading Bi_2Te_3 plates between the graphene sheets. The graphene content is roughly estimated to be 11.5 wt% by the carbon content analysis.

To check the reduction status of GO during the solvothermal reactions, C1s XPS spectra of GO and Bi_2Te_3/G are analyzed as shown in Figure 1b. The spectra can be fitted by four peaks for different forms of carbons: non-oxygenated carbon (C-C, 285.6 eV and C=C, 284.8 eV), carbon in C-O bonds (286.3 eV), carbonyl carbon (C=O, 287.6 eV) and carboxylate carbon (O-C=O, 289.0 eV) [28]. After the solvothermal reactions, the peak intensity of the oxygenated carbons (C-O, C=O, O-C=O) shows an obvious decrease, indicating the reduction of GO into graphene. Figure 1c gives the O1s XPS

spectra of the hybrid. The broad peak at 532.2 eV is assigned to the residual oxygen-containing groups such as -COOH and -OH [29], which agrees with the result of C1s spectra. From the XRD and XPS analyses, it can be concluded that a Bi_2Te_3/G hybrid has formed with the simultaneous formation Bi_2Te_3 and reduction of GO during the one-step solvothermal process.

Figure 1. (**a**) XRD of Bi_2Te_3/G and bare Bi_2Te_3; (**b**) C1s XPS of GO and Bi_2Te_3/G; (**c**) O1s XPS of Bi_2Te_3/G.

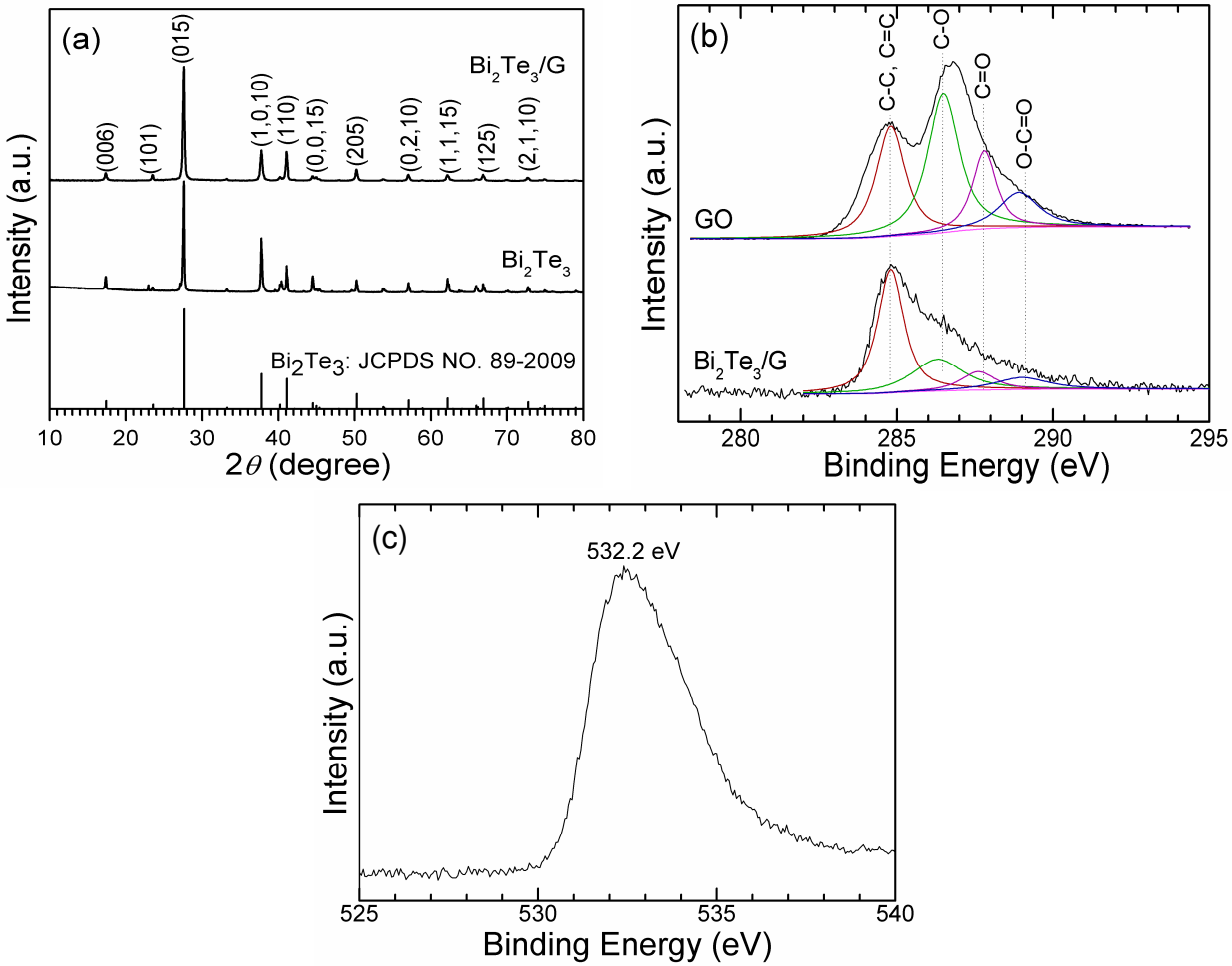

Figure 2a shows the SEM image of bare Bi_2Te_3 prepared by the solvothermal route without adding GO in the precursors. Generally, the sample exhibits a hexagonal plate shape with a size of around 0.5–3 μm. However, smaller sized broken plates with an irregular shape can also be observed. The thickness of the plates is roughly estimated to be 50–100 nm from some vertically (or partially vertically) aligned plates denoted by the arrows. Figure 2b shows the SEM image of the Bi_2Te_3/G hybrid. It is obvious from the transparent graphene that Bi_2Te_3 plates are located between the graphene sheets. The size of the Bi_2Te_3 plates is below 2 μm. A three-dimensional (3D) sandwich structure is thus constructed by alternatively arranged graphene layer and Bi_2Te_3 layer as clearly indicated by the arrows. The transparent nature of the graphene layer suggests that it is rather thin, composed probably of single or few layers of graphene sheets.

The microstructure of Bi_2Te_3/G was further characterized by TEM as shown in Figure 2c. Note that nearly all of the Bi_2Te_3 plates are anchoring on graphene without forming free Bi_2Te_3 plates even after

vigorous ultrasonication. The wrinkles and folded edges of graphene indicate that the graphene layer is rather thin, which agrees with the SEM observation. The enlarged view of the circled part in Figure 2c is presented in Figure 2d. The overlapping of the Bi_2Te_3 plates can be observed from Figure 2d, from which the transparent nature of the Bi_2Te_3 plate is evident. From a vertically aligned plate, the thickness of the plate is estimated to be 15 nm, which is much smaller compared with that of bare Bi_2Te_3. The thickness of the Bi_2Te_3 plates is in the range of 10–20 nm after observing some plates at the edges or defect sites of graphene. It is worth noting that the number of the Bi_2Te_3 plates with a regular hexagon is much smaller compared with that of bare Bi_2Te_3 plates. It is believed that the irregular shape and small thickness of the Bi_2Te_3 plates in Bi_2Te_3/G are caused by the inhibited diffusion and re-crystallization of small sized Bi_2Te_3 particles due to the pinning effect of the defects and the oxygen-containing groups in graphene [30]. The presence of the residual oxygen-containing groups can be confirmed by XPS shown in Figure 1b,c.

Figure 2. (**a**) SEM image of bare Bi_2Te_3; (**b**) SEM image of Bi_2Te_3/G hybrid; (**c**) TEM image of Bi_2Te_3/G hybrid; (**d**) the enlarged view of the circled part in (**c**).

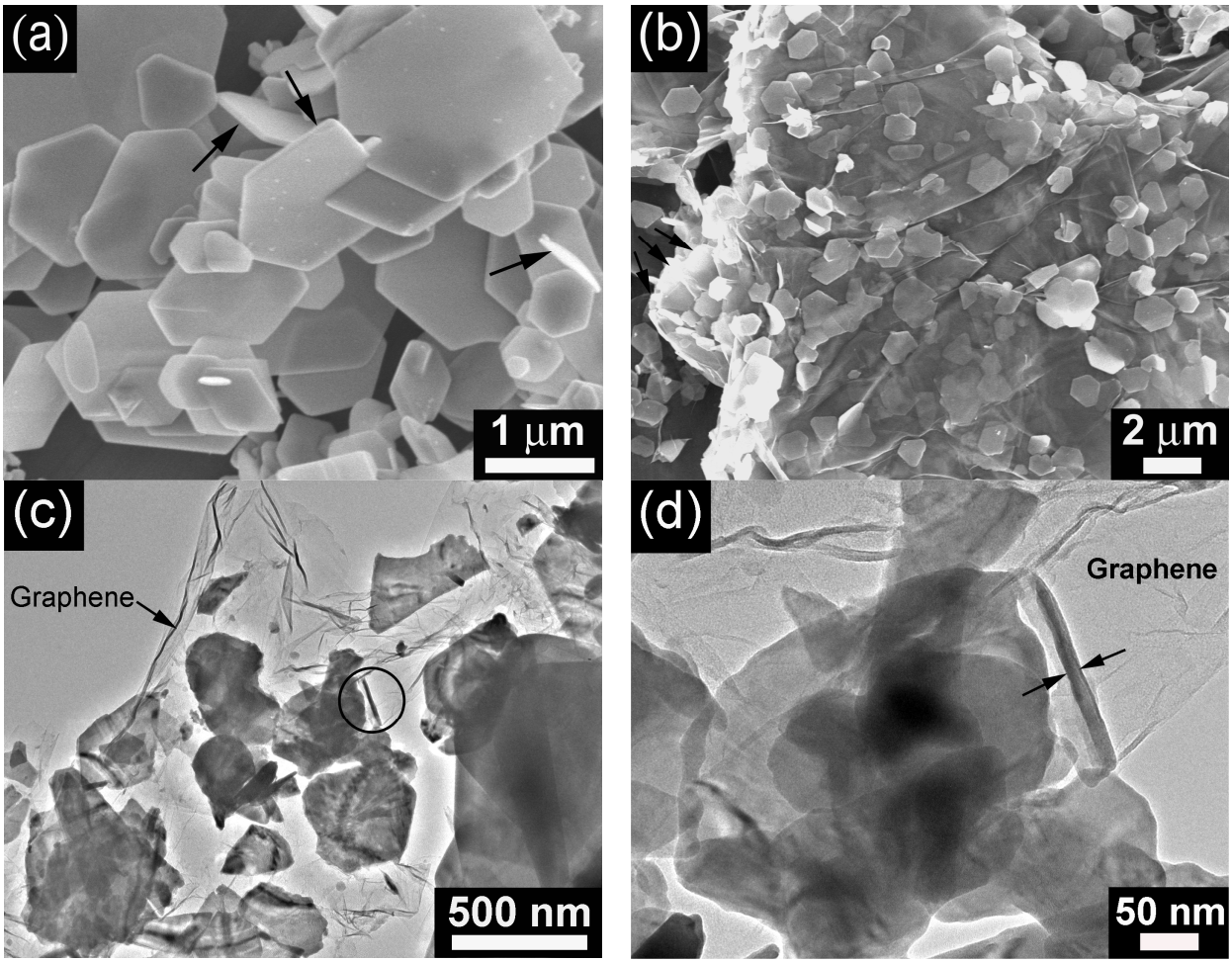

In Figure 3, CV plots of Bi_2Te_3/G and Bi_2Te_3 were measured to clarify the electrochemical reaction mechanism of Bi_2Te_3 with Li. As seen in Figure 3a, the reaction Bi_2Te_3 with Li exhibits a multi-step mechanism, evidenced by the multi-peak feature of the CV plots. During the first cathodic scan, three reduction peaks, located at 2.0, 1.25, and 0.6 V, respectively, appear as indicated by the black line in

Figure 3a. The small peak at 2.0 V is related possibly to the insertion reaction of Li ion into layered Bi_2Te_3 without significantly destroying its crystal structure [31]. The peak at 1.2 V corresponds to the lithiation reaction of Te by forming Li_2Te ($2Li + Te \rightarrow Li_2Te$) [27], and the peak at 0.6 V is associated with the reaction of Bi with Li to form Li_3Bi ($3Li + Bi \rightarrow Li_3Bi$) [5,26,27]. During the second cathodic scan, the peak at 2.0 V almost disappears, the peak at 0.6 V is shifted to a higher value of 0.7 V (A'), while the peak at 1.2 V is divided into two peaks, B' and C', located at 1.35 and 1.65 V, respectively. The division of the peak means that the reaction of Te with Li occurs via a two-step mechanism by forming $LiTe_3$ and Li_2Te successively, both of which are stable phases at room temperature [32]. The lower peak potential in the first cathodic scan compared with those in the subsequent scans is due to the additional energy required for the displacement reactions of Bi_2Te_3 upon Li uptake [4]. This also means that structure of Bi_2Te_3 cannot be recovered after the anodic scan [27].

Note that three oxidation peaks (A, B, and C), at 1.0, 1.8 and 1.9 V, respectively, appear during the anodic scans, corresponding to the successive de-lithiation reactions of Li_3Bi (peak A) and Li_2Te (peak B and peak C). The CV plots of bare Bi_2Te_3 are also given for comparison as seen in Figure 3b. The plots of bare Bi_2Te_3 display a similar feature as those of Bi_2Te_3/G except that the peak intensity decreases more rapidly with scans, indicative of its lower reversibility. The relatively high reversibility of Bi_2Te_3/G can be attributed to the incorporation of graphene that improves the electrode kinetics and keeps the electrode integrity.

Figure 3. CV plots of (**a**) Bi_2Te_3/G; and (**b**) Bi_2Te_3 scanned at 0.1 mV s^{-1}.

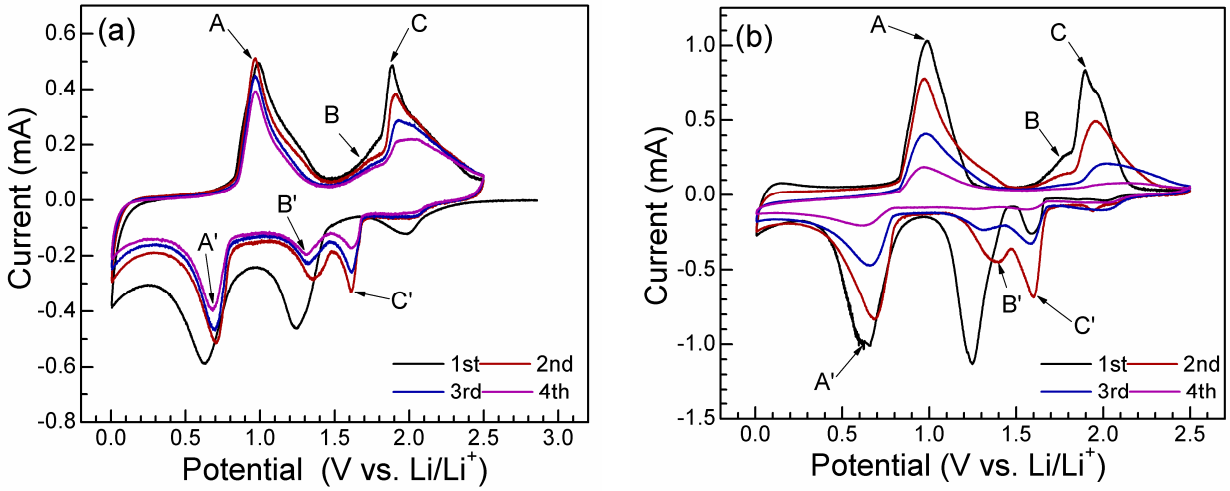

Figure 4a shows the chare-discharge curves of Bi_2Te_3 and Bi_2Te_3/G at 50 mA g^{-1} at various cycles. Bi_2Te_3/G hybrid gives a first discharge (Li-uptake) capacity of 731 mAh g^{-1} and a first charge (Li-extraction) capacity of 481 mAh g^{-1}. The first irreversible capacity can be attributed to the reduction decomposition of the electrolyte and the formation of the solid state interface (SEI) layer. Successive potential plateaus can be seen during the charge-discharge cycling, which correspond to the current peaks in the CV plots. The appearance of the potential plateaus is due to the two-phase coexistence of original phase (Te or Bi) and the Li-alloys (Li-Te or Li-Bi alloys). As shown in the figure, bare Bi_2Te_3 exhibits lower charge-discharge capacities compared with Bi_2Te_3/G. The theoretical maximum capacity of Bi_2Te_3 is 401 mAh g^{-1}, related to the formation of Li_2Te and Li_3Bi.

Considering the fact that graphene itself shows a relatively low capacity of around 300 mAh g^{-1}, as reported in our previous work [33], the theoretical capacity of Bi_2Te_3/G should be lower than that of bare Bi_2Te_3. The high yieldable of Bi_2Te_3/G is possibly due to the synergistic effect between Bi_2Te_3 and graphene. On one hand, as discussed above, the presence of graphene can restrain the crystal growth of Bi_2Te_3, which is favorable for rapid Li ion diffusion within the active material. On the other hand, the separator effect of Bi_2Te_3 plates for graphene sheets maximizes the exposure of the graphene surface to the electrolyte, especially for the edges and vacancies on graphene. The edges and vacancies can supply additional sites for Li storage [34]. Note that Bi_2Te_3/G shows a progressive polarization upon cycling, but the extent is smaller than bare Bi_2Te_3 owing to the presence of the conductive graphene.

Figure 4b compares the cycling stability between bare Bi_2Te_3 and Bi_2Te_3/G charged at 50 and 200 mA g^{-1} and discharged at 50 mA g^{-1}. Note that Bi_2Te_3/G demonstrates an obviously slower capacity fade compared to bare Bi_2Te_3. After 50 cycles at 200 mA g^{-1} (about 0.5 C), a charge capacity of 158 mAh g^{-1} can be retained for Bi_2Te_3/G. In contrast, the charge capacity of bare Bi_2Te_3 drops rapidly to 33 mAh g^{-1}. The Bi_2Te_3/G hybrid also shows improved cycling stability compared with Bi_2Te_3-graphite composite [27] and other Bi-based anodes [25,26]. The enhanced cycling stability is attributed to the buffering effect of graphene that alleviates the large volume changes and the confinement effect of graphene that restrains the aggregation of the Bi_2Te_3 plates, in addition to offering effective conducting networks. The 3D sandwich structure also facilitates the Li-ion diffusion within the free space and across the electrode/electrolyte interface. In addition, the free space within the sandwich also affords additional room to buffer the volume changes. It should be stressed that the long-term cycling stability of the Bi_2Te_3/G hybrid is not satisfactory yet owing to the intrinsic large volume changes of the Bi_2Te_3 during alloying/de-alloying processes. However, it is clear that graphene plays an important role in enhancing the electrochemical properties of Bi_2Te_3. It also should be noted that the large-scaled of Bi_2Te_3/G is not favored due to the toxicity, price, and resource scarcity of Bi and Te. Nevertheless, it shows promising application in micro-batteries due to the possibility of micro processing of graphene and Bi_2Te_3.

Figure 4. (**a**) Voltage profiles; and (**b**) cycling stability of Bi_2Te_3/G and Bi_2Te_3.

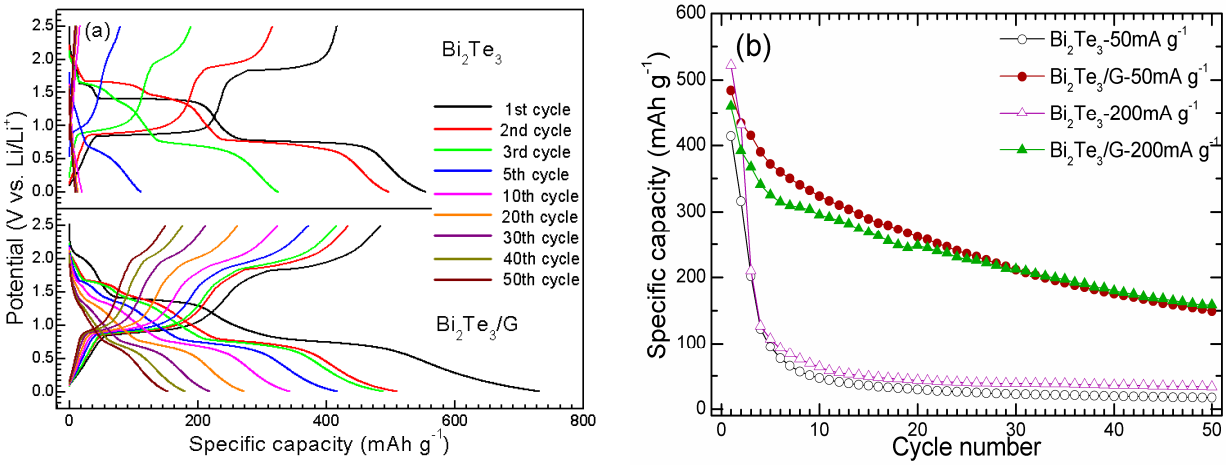

3. Experimental Section

3.1. Preparation of Bi_2Te_3-Nanoplate/Graphene-Nanosheet (Bi_2Te_3/G) Nanohybrid

Graphite oxide (GO, 80 mg), prepared by a modified Hummer's method [35], was added into 40 mL of ethylene glycol (EG) and sonicated for 24 h to obtain a sufficiently exfoliated GO suspension. Then, 1 mmol of $BiCl_3$, 1.5 mmol of Na_2TeO_3 and 0.4 g of NaOH was added to the above suspension with sonication. After stirring for 12 h, the mixed solution was then transferred to a Teflon-lined stainless steel autoclave (100 mL) and heated in an electric oven at 180 °C for 24 h. The as-obtained product was collected by centrifugation, washed with deionized water and absolute ethanol for several times and dried at 40 °C under vacuum for 10 h. Bare Bi_2Te_3 was also synthesized using a similar method without adding GO.

3.2. Materials Characterization

The X-ray diffraction (XRD) patterns were obtained on a Rigaku D/Max-2550pc powder diffractometer using Cu K_α radiation (λ = 0.1541 nm). X-ray photoelectron spectra (XPS) were collected on a KRATOS AXIS ULTRA-DLD spectrometer with a monochromatic Al K_α radiation ($h\nu$ = 1486.6 eV). The morphologies of the products were observed by field emission scanning electron microscopy (FE-SEM) on a FEI-sirion microscope and transmission electron microscopy (TEM) on a JEM 2100F microscope. The carbon content analysis was conducted on a Flash EA 1112 tester.

3.3. Electrochemical Measurements

The electrochemical measurements of Bi_2Te_3/G and Bi_2Te_3 were performed with a half-cell configuration using CR2025-type coin cells. The working electrodes were prepared by spreading a slurry composed of 75 wt% active material (Bi_2Te_3/G or Bi_2Te_3/G), 15 wt% poly(vinylidene fluoride) (PVDF) and 10 wt% acetylene black onto Ni foam followed by drying at 100 °C for 12 h under vacuum. The loading mass of the active material is around 2 mg. The cells were assembled in an Ar-filled glove box using Li foil as the counter electrode and Celgard 2300 membrane as the separator. The electrolyte used was 1 M $LiPF_6$ in ethylene carbonate (EC)/dimethyl carbonate (DMC) (volume ratio 1:1). The cells were galvanostatically charged-discharged at 50 mA g^{-1} between 0.005 and 2.5 V *vs.* Li/Li^+ on a Neware battery tester (Shenzhen, China). The specific capacity of Bi_2Te_3/G was calculated based on the total weight of Bi_2Te_3 and graphene. Cyclic voltammetry (CV) tests were carried out on an Arbin BT2000 system at a scan rate of 0.1 mV s^{-1} between 0.005 and 2.5 V *vs.* Li/Li^+. All of the electrochemical measurements were carried out at room temperature.

4. Conclusions

The Bi_2Te_3/G sandwich has been prepared by an in situ route with alternatively arranged Bi_2Te_3 nanoplates and graphene nanosheets. The diffusion and re-crystallization of Bi_2Te_3 in Bi_2Te_3/G are inhibited due to presence of oxygen-containing groups and defects on graphene, leading to more irregular shape and smaller thickness of Bi_2Te_3 in Bi_2Te_3/G compared with those in bare Bi_2Te_3. Both Bi_2Te_3/G and Bi_2Te_3 exhibit a multi-step lithiation mechanism. The Bi_2Te_3/G hybrid can yield a

higher-than-the-theoretical charge capacity of mAh h^{-1} at 50 mA g^{-1} due to the synergistic effect between Bi_2Te_3 and graphene. The Bi_2Te_3/G hybrid shows an obviously improved cycling stability compared with bare Bi_2Te_3. The improved cycling stability is attributed to the 3D sandwich structure, where graphene not only buffers the volume changes but also immobilizes Bi_2Te_3 nanoplates, in addition to offering effective conducting networks. The unique sandwich structure also facilitates Li-ion diffusion at the electrode/electrolyte interface and within the free space of the sandwich.

Acknowledgments

This work was supported by the National Natural Science Foundation of China (No. 51101139), the Ph.D. Programs Foundation of Ministry of Education of China (No. 20100101120024), the Foundation of Education Office of Zhejiang Province (No. Y201016484), the Qianjiang Talents Project of Science Technology Department of Zhejiang Province (2011R10021), and Key Science and Technology Innovation Team of Zhejiang Province under grant number 2010R50013.

References

1. Tarascon, J.M.; Armand, M. Issues and challenges facing rechargeable lithium batteries. *Nature* **2001**, *414*, 359–367.
2. Poizot, P.; Laruelle, S.; Grugeon, S.; Dupont, L.; Tarascon, J.M. Nano-sized transition-metal oxides as negative-electrode materials for lithium-ion batteries. *Nature* **2000**, *407*, 496–499.
3. Tirado, J.L. Inorganic materials for the negative electrode of lithium ion batteries: State-of-the-art and future prospects. *Mater. Sci. Eng. R* **2003**, *40*, 103–136.
4. Zhang, W.J. Lithium insertion/extraction mechanism in alloy anodes for lithium-ion batteries. *J. Power Sources* **2011**, *196*, 877–887.
5. Huggins, R.A. Lithium alloy negative electrodes. *J. Power Sources* **1999**, *81–82*, 13–19.
6. Obrovac, M.N.; Christensen, L.; Le, D.B.; Dahn, J.R. Alloy design for lithium-ion battery anodes. *J. Electrochem. Soc.* **2007**, *154*, A849–A855.
7. Alcántara, R.; Fernández-Madrigal, F.J.; Lavela, P.; Tirado, J.L.; Jumas J.C.; Olivier-Fourcade, J. Electrochemical reaction of lithium with the $CoSb_3$ skutterudite. *J. Mater. Chem.* **1999**, *9*, 2517–2521.
8. Park, C.M.; Sohn, H.J. Antimonides ($FeSb_2$, $CrSb_2$) with orthorhombic structure and their nanocomposites for rechargeable Li-ion batteries. *Electrochim. Acta* **2010**, *55*, 4987–4994.
9. Villevieille, C.; Ionica-Bousquet, C.M.; Ducourant, B.; Jumas, J.C.; Monconduit, L. $NiSb_2$ as negative electrode for Li-ion batteries: An original conversion reaction. *J. Power Sources* **2007**, *172*, 388–394.
10. Park, C.M.; Sohn, H.J. Electrochemical characteristics of $TiSb_2$ and Sb/TiC/C nanocomposites as anodes for rechargeable Li-ion batteries. *J. Electrochem. Soc.* **2010**, *157*, A46–A49.
11. Xie, J.; Zhao, X.B.; Cao, G.S.; Zhao, M.J.; Su, S.F. Solvothermal synthesis and electrochemical performances of nanosized $CoSb_3$ as anode materials for Li-ion batteries. *J. Power Sources* **2005**, *140*, 350–354.
12. Xie, J.; Zhao, X.B.; Cao, G.S.; Zhong, Y.D.; Zhao, M.J.; Tu, J.P. Solvothermal synthesis of nanosized $CoSb_2$ alloy anode for Li-ion batteries. *Electrochim. Acta* **2005**, *50*, 1903–1907.

13. Sarakonsri, T.; Johnson, C.S.; Hackney, S.A.; Thackeray, M.M. Solution route synthesis of InSb, Cu_6Sn_5 and Cu_2Sb electrodes for lithium batteries. *J. Power Sources* **2006**, *153*, 319–327.
14. Kim, H.; Cho, J. Template synthesis of hollow Sb nanoparticles as a high-performance lithium battery anode material. *Chem. Mater.* **2008**, *20*, 1679–1681.
15. Chen, W.X.; Lee, J.Y.; Liu, Z.L. The nanocomposites of carbon nanotube with Sb and $SnSb_{0.5}$ as Li-ion battery anodes. *Carbon* **2003**, *41*, 959–966.
16. Hassoun, J.; Derrien, G.; Panero, S.; Scrosati, B. The role of the morphology in the response of Sb–C nanocomposite electrodes in lithium cells. *J. Power Sources* **2008**, *183*, 339–343.
17. He, Y.; Huang, L.; Li, X.; Xiao, Y.; Xu, G.L.; Li, J.T.; Sun, S.G. Facile synthesis of hollow Cu_2Sb@C core-shell nanoparticles as a superior anode material for lithium ion batteries. *J. Mater. Chem.* **2011**, *21*, 18517–18519.
18. Applestone, D.; Yoon, S.; Manthiram, A. Mo_3Sb_7-C composite anodes for Lithium-ion batteries. *J. Phys. Chem. C* **2011**, *115*, 18909–18915.
19. Novoselov, K.S.; Geim, A.K.; Morozov, S.V.; Jiang, D.; Zhang, Y.; Dubonos, S.V.; Grigorieva, I. V.; Firsov, A.A. Electric filed effect in atomically thin carbon films. *Science* **2004**, *306*, 666–669.
20. Park, S.; An, J.H.; Jung, I.W.; Piner, R.D.; An, S.J.; Li, X.S.; Velamakanni, A.; Ruoff, R.S. Colloidal suspensions of highly reduced graphene oxide in a wide variety of organic solvents. *Nano Lett.* **2009**, *9*, 1593–1597.
21. Stoller, M.D.; Park, S.; Zhu, Y.W.; An, J.H.; Ruoff, R.S. Graphene-based ultracapacitor. *Nano Lett.* **2008**, *8*, 3498–3502.
22. Lee, C.; Wei, X.D.; Kysar, J.W.; Hone, J. Measurement of the elastic properties and intrinsic strength of monolayer graphene. *Science* **2008**, *321*, 385–388.
23. Xie, J.; Zheng, Y.X.; Pan, R.J.; Liu, S.Y.; Song, W.T.; Cao, G.S.; Zhu, T.J.; Zhao, X.B. Sb-based alloy (NiSb, $FeSb_2$) nanoparticles decorated graphene prepared by one-step solvothermal route as anode for Li-ion batteries. *Int. J. Electrochem. Sci.* **2011**, *6*, 4811–4821.
24. Zheng, Y.X.; Xie, J.; Liu, S.Y.; Song, W.T.; Cao, G.S.; Zhu, T.J.; Zhao, X.B. Self-assembly of Co-Sb-nanocrystal/graphene hybrid nanostructure with improved Li-storage properties via a facile *in situ* solvothermal route. *J. Power Sources* **2012**, *202*, 276–283.
25. Crosnier, O.; Devaux, X.; Brousse, T.; Fragnaud, P.; Schleich, D.M. Influence of particle size and matrix in "metal" anodes for Li-ion cells. *J. Power Sources* **2001**, *97–98*, 188–190.
26. Pérez-Flores, J.C.; Kuhn, A.; García-Alvarado, F. Electrochemical performances of $BiSbO_4$ as electrode material for lithium batteries. *J. Power Sources* **2008**, *182*, 365–369.
27. Zhao, X.B.; Cao, G.S.; Lv, C.P.; Zhang, L.J.; Hu, S.H.; Zhu, T.J.; Zhou, B.C. Electrochemical properties of some Sb or Te based alloys for candidate anode materials of lithium-ion batteries. *J. Alloys Compd.* **2001**, *315*, 265–269.
28. Shin, H.J.; Kim, K.K.; Benayad, A.; Yoon, S.M.; Park, H.K.; Jung, I.S.; Jin, M.H.; Jeong, H.K.; Kim, J.M.; Choi, J.Y.; Lee, Y.H. Efficient reduction of graphite oxide by sodium borohydride and its effect on electrical conductance. *Adv. Funct. Mater.* **2009**, *19*, 1987–1992.
29. Wu, Z.S.; Ren, W.C.; Wen, L.; Gao, L.B.; Zhao, J.P.; Chen, Z.P.; Zhou, G.M.; Li, F.; Cheng, H.M. Graphene anchored with Co_3O_4 nanoparticles as anode of lithium ion batteries with enhanced reversible capacity and cyclic performance. *ACS Nano* **2010**, *4*, 3187–3194.

30. Wang, H.L.; Robinson, J.T.; Diankov, G.; Dai, H.J. Nanocrystal growth on graphene with various degrees of oxidation. *J. Am. Chem. Soc.* **2010**, *132*, 3270–3271.
31. Chen, J.K.; Sun, Z.L.; Zhu, Y.J.; Chen, N.F.; Zhou, Y.F.; Ding, J.; Chen X.H.; Chen, L.D. Top-down fabrication of nano-scaled $Bi_2Se_{0.3}Te_{2.7}$ associated by electrochemical Li intercalation. *Dalton Trans.* **2011**, *40*, 340–343.
32. Cunningham, P.T.; Johnson, S.A.; Cairns, E.J. Phase equilibria in lithium-chalcogen systems. *J. Electrochem. Soc.* **1973**, *120*, 328–330.
33. Liu, S.Y.; Xie, J.; Zheng, Y.X.; Cao, G.S.; Zhu, T.J.; Zhao, X.B. Nanocrystal manganese oxide (Mn_3O_4, MnO) anchored on graphite nanosheet with improved electrochemical Li-storage properties. *Electrochim. Acta* **2012**, *66*, 271–278.
34. Pan, D.Y.; Wang, S.; Zhao, B.; Wu, M.H.; Zhang, H.J.; Wang, Y.; Jiao Z. Li storage properties of disordered graphene nanosheets. *Chem. Mater.* **2009**, *21*, 3136–3142.
35. Hummers, W.S.; Offeman, R.E. Preparation of graphitic oxide. *J. Am. Chem. Soc*. **1958**, *80*, 1339–1339.